Biointerface Research in Applied Chemistry
Open-Access Journal (ISSN: 2069-5837)

Article
Volume 13, Issue 6, 2023, 554
https://doi.org/10.33263/BRIAC136.554

Survey of Fe_3O_4 Magnetic Nanoparticles Modified with Sodium Dodecyl Sulfate for Removal P-Cresol and Pyrocatechol from Aqueous Solutions

Ferdos Kord Mostafapour [1], Amin Miri [2], Aramdokht Khatibi [1], Davoud Balarak [1,*], George Z. Kyzas [3,*]

[1] Department of Environmental Health, Health Promotion Research Center, Zahedan University of Medical Sciences, Zahedan, Iran; ferdoskord@gmail.com (F.K.M.); adokhtkhatibi@gmail.com (A.K.); dbalarak2@gmail.com (D.B.);
[2] Student Research Committee, Zahedan University of Medical Sciences, Zahedan, Iran; dbchemistry2@gmail.com (A.M.);
[3] Department of Chemistry, International Hellenic University, Kavala, Greece; kyzas@chem.ihu.gr (G.Z.K.);
* Correspondence dbalarak2@gmail.com (D.B.); kyzas@chem.ihu.gr (G.Z. K.);

Scopus Author ID 55928067100 (D.B.)
17345938100 (G.Z.K.)

Received: 3.11.2022; Accepted: 5.01.2023; Published: 24.02.2023

Abstract: Phenolic compounds have been introduced to be toxic, carcinogenic, mutagenic, and teratogenic, and they have adverse effects on the nervous, cardiovascular, and respiratory systems. This research aimed to scrutinize the efficiency of Fe_3O_4 nanoparticles modified with sodium dodecyl sulfate (Fe_3O_4/SDS) to remove p-cresol and pyrocatechol from an aqueous environment. The maximum elimination efficiencies at neutral pH were 98.9% for pyrocatechol and 91.2% for p-cresol. This percentage was obtained at a pH equal to 7, contact time of 60 min, p-cresol and pyrocatechol concentration of 50 mg/L, and Fe_3O_4/SDS dose of 0.4 g/L and at a temperature of 30 ℃. Equilibrium data were analyzed with four linear and nonlinear isotherm and kinetic models and four error coefficient models. The results showed the compliance of the data with the Langmuir isotherm for both the samples and with both linear and nonlinear models. Furthermore, thermodynamic studies ascertained that the p-cresol and pyrocatechol adsorption on the adsorbent is spontaneous and endothermic. Adsorption tests in three consecutive cycles showed a 4% reduction in removing p-cresol and pyrocatechol. Finally, it can be said that Fe_3O_4/SDS has high efficiency in removing phenolic compounds from aqueous environments, and it can be easily collected from the system by a magnetic adsorbent.

Keywords: Fe_3O_4/SDS; pyrocatechol; p-cresol; adsorption; sodium dodecyl sulfate.
Abbreviation and Nomenclature: EPA= Environmental Protection Agency; WHO=World Health Organization; SDS=Sodium dodecyl sulfate; CTAB=Cetyltrimethylammonium bromide; CPC= cetylpyridinium chloride; DODMAC= Dioctadecyldimethylammonium chloride; D-R=Dubinin-Radushkevich; PSO=Pseudo-second-order; PFO= Pseudo-first-order; SEM= Scanning electron microscope; XRD= X-ray powder diffraction; VSM= Vibrating Sample Magnetometer; FTIR= Fourier Transform Infrared Spectrometer; pH_{PZC}= Point of zero charge; IPD=Intra-particle diffusion; ΔG^o= Free energy change (kJ/mol); ΔH^o= Enthalpy change (kJ/mol); ΔS^o= Entropy change (kJ/mol. K); $C_{0=}$ initial concentration of pyrocatechol and p-cresol (mg/g); $C_{t=}$ concentration at equilibrium (after adsorption) (mg/L); C_{ads} = amount of target pollutants (mg/g); R= universal gas constant (8.314 J/mol.K); T= absolute temperature (K); M=adsorbent mass (g); V=volume of pyrocatechol and p-cresol solution (L); AC=activated carbon.

1. Introduction

To achieve sustainable development, paying attention to environmental management is inevitable [1, 2]. One of the important issues that threaten the environment's health is resistant and toxic compounds that enter the environment through industrial wastewater [3]. Natural processes, including the decomposition of organic matter, incomplete combustion of wood and coal, and wastewater from oil refineries and landfill sites, lead to the production of phenols and transfer their permanent pollution to water, body, and soil [4, 5]. Phenolic compounds are found in glass-making industries, solvent production, explosives production, petrochemicals, food industry, fertilizer processes, textile industries, waste and paper disposal equipment, polymer resins, and medicinal plants [6]. The highest amount of phenolic compounds and the most toxic phenolic compound is 4-methyl phenol or para-cresol, called p-cresol [7]. The amount of p-cresol production in the environment is significantly high. It enters the human body through various ways, such as inhalation, water, air, and food, such as tea leaves, oil, and tomatoes [8, 9]. Phenolic compounds in high concentrations are toxic, carcinogenic, mutagenic, and teratogenic; in low concentrations, they have adverse effects on the nervous, cardiovascular and respiratory systems [10, 11]. The toxicity of cresol in the human body is linked to its hydrophobic behavior and its transformation into binary active compounds or the production of free radicals [12]. These intermediate compounds come into contact with the cells and tissues of the human body and lead to cell destruction. P-Cresol is chemically and biologically resistant and is classified by the US EPA as a priority pollutant in Group C (probably carcinogenic to humans) [13]. The WHO recommends a concentration of 0.001 mg/L as an admissible concentration of p-cresol in drinking water. Hence, an imperative need to reduce the concentration of p-cresol to an acceptable level before the discharge of contaminated wastewater into water is perceived [14, 15]. Catechol, a cyclic organic compound with high toxicity, enters the environment through various industries such as pharmaceuticals, poison, and pesticide production, oil production, plastic manufacturing, and wood and paper industries, damaging human health and the health of the environment [16, 17]. Catechol is easily absorbed by the digestive system and causes the breakdown of red blood cells, destruction of the digestive system, and subsidence of vital activities [18].

Eliminating phenolic compounds (e.g., p-cresol and catechol) is done by physical and chemical processes such as solvent extraction, adsorption, chemical oxidation, and burning, which lead to relatively high operating costs and the production of dangerous byproducts [19, 20]. One of the most operative processes employed to eliminate pollutants is adsorption, which is more popular due to its low cost and comfort of use [21]. The large surface area, microporous structure, and high adsorption capacity of the activated carbon provided the most acceptability and favorability for its employment in removing pollutants from wastewater; despite its attractiveness, issues associated with costs restrict its use [22, 23]. Developing cost-effective adsorbents through employing clay materials, zeolites, siliceous material, industrial waste products, agricultural wastes, and biosorbents such as chitosan and peat has lately become the objective of numerous researchers [24, 25].

Much attention has been recently paid to employing magnetic separation in various areas, including removal, isolation, and/or concentration of desired components from solutions [26]. In different studies, considering the nanosized magnetic iron oxide particles' large surface area and small diffusion resistance for separating and removing chemicals such as metals, dyes, and gases, they were examined as new adsorbents [27].

Currently, hydrothermal synthesis, co-precipitation, microemulsion, and thermal decomposition have been identified as methods employed in preparing the Fe_3O_4 nanoparticles (NPs) [28]. However, co-precipitation has been found to be a simplistic and practical method; this method leads to synthesizing iron oxides from aqueous Fe^{2+}/Fe^{3+} salt solutions in the presence of a base; the prepared iron oxide has depicted high efficiency and a comparatively narrow size distribution [29]. Since NPs have a large surface area to volume ratios, agglomeration for reducing surface energy is observed for them, and modification of their surface has been introduced as a solution to overwhelming this problem [30]. Generally, considering the application of these particles, covering their surface through physical and/or chemical adsorption of the preferred molecules is performed to modify their surface [31, 32].

The modifying surface of Fe_3O_4 NPs by SDS, CTAB, CPC, and DODMAC, which are ionic surfactants, leads to forming hemimicelles and micelles. There are two central characteristics, i.e., the hydrophobic (outer surface of hemimicelles) and ionic surfaces. Hence, surfactant-coated Fe_3O_4 NPs are an innovative adsorbent that adsorbs different pollutants through electrostatic and hydrophobic interaction [33, 34].

Therefore, considering the importance and environmental problems caused by p-cresol and catechol and the high efficiency of Fe_3O_4/SDS in the treatment of pollutants, in our study, we were looking to determine the efficiency of magnetic iron oxide nanoparticles modified with sodium dodecyl sulfate in removing p-cresol and pyrocatechol from aqueous solutions.

2. Materials and Methods

2.1. Chemical and reagents.

Pyrocatechol and p-cresol as target pollutants were purchased from Sigma Aldrich Co. SDS, sodium hydroxide, Ferric chloride ($FeCl_3.6H_2O$), ferrous chloride ($FeCl_2.4H_2O$), methanol, dichloromethane, Propanol, Sodium carbonate, and HCl were provided by Merck, co. Germany. All chemicals were of analytical grade. In preparing all solutions, double distilled water was employed. A standard stock solution of catechol and p-cresol (1000 mg/L) was made in double distilled water. Using distilled water, other solutions (5, 10, 25 and 50, and 100 mg/L) were prepared with diluting standard solution. These solutions were employed in studies to optimize effective parameters and plot the calibration curve for calculating the catechol and p-cresol removal efficiency with GC.

2.2. Synthesis of nanoparticles.

A chemical co-precipitation method was employed in the present work to prepare Fe_3O_4 NPs. The method mentioned below is concise: by dissolving 10.4 g of $FeCl_3.6H_2O$, 4.0 g of $FeCl_2.4H_2O$, and 1.7 mL of HCl (12 mol/L) in 50 mL of deionized water, the stock solution of ferrous and ferric chloride in a beaker was prepared. They then underwent the degassing process with nitrogen gas for 20 min. Meanwhile, 1.5 mol/L NaOH solution (500 mL) underwent degassing (15 min) and heating process at 80 °C. After that, instilling stock solution using the dropping funnel was done for 30 min under nitrogen gas protection; a glassware stirrer performed this during strong stirring (1000 rpm). All the above procedures were accomplished under a fixed solution temperature of 80 °C. Purging nitrogen gas was considered to stop the intrusion of oxygen. The formation of MNPs was carried out based on the following reaction:

$$Fe^{2+} + 2Fe^{3+} + 8OH- \rightarrow Fe_3O_4 + 4H_2O$$

The Fe_3O_4 NPs precipitate obtained in the mentioned reaction was then withdrawn by the magnetic field from the reaction environment. Then, the rinsing process for them was applied four times with deionized water (500 mL). Eventually, re-suspension of prepared Fe_3O_4 NP was done in degassed deionized water (500 mL). After the washings, the pH of the suspension was measured to be 11.0. Moreover, in suspension, the levels of synthesized NPs were valued to be 10 mg /mL.

The washing process with distilled water was repeated several times to remove ammonia and lower the pH to about 7 completely. Finally, the sediment obtained was added to 15 ccs of distilled water to disperse the particles in the target fluid. The samples that were poured into the water were ultrasonically treated for 5 minutes. Sodium dodecyl was added to the nanoparticles to form a double layer on the nanoparticles' surface and facilitate the magnet's collection of nanoparticles. The physical and structural features of the synthesized adsorbent were explored using SEM, XRD, VSM, and FTIR techniques.

2.3. Optimization of parameters.

This is an experimental-laboratory study, and it was done in the batch mood. In order to perform the experiments, first, a stock solution (1000 mg/L) was prepared, and this solution was used to make the preferred concentrations. In this research, the effect of parameters, i.e., solution pH (3, 5, 7, 9, and 11), adsorbent mass (0.1, 0.2, 0.4, 0.6, and 0.8 g/L), initial concentration pyrocatechol and p-cresol (5,10, 25, 50, and 100 mg/L), reaction contact time (10, 20, 30, 45, 60, 75, 90 and 120 min) and reaction temperature (20, 30, 40, and 50 °C) was performed on the reduction of pyrocatechol and p-cresol. To optimize these parameters, the pH of the solutions was first optimized, and then by keeping the optimized parameter constant, the other parameters were optimized in order. First, 0.5 L of pyrocatechol solution (25 mg/L) was prepared, and the 100 ml sample was transferred to 5 Erlenmeyer flasks (a capacity of 200 ml). After that, 0.4 g/L (0.04 g) of Fe_3O_4 nanoparticles and 1 ml of sodium dodecyl sulfate were added to each container and placed in a shaker incubator at 30 ℃ for 60 min. After the set time, the samples were taken out, and the nanoparticles were separated by a magnet. 0.5 g of sodium carbonate was added to extract the samples for injection into the gas chromatography machine. Then 10 mL of each sample was taken and transferred into plastic vials, and 2 ml of dichloromethane and 1 ml of propanol were added to all samples. The vials were placed on a shaker for 10 minutes and then centrifuged at 4000 rpm for 5 minutes. Then, a sampler removed 1 microliter of the extraction solvent from each sample and injected into the gas chromatography (GC) machine. The residual concentration of pyrocatechol was calculated according to the peak area of each sample, and the removal efficiency and adsorption capacity were calculated using formulas no. 1 and 2 [35, 36].

$$\text{Efficiency} = (C_0 - C_t)/ C_t) \times 100 \quad (1)$$

$$Q_e = (Co\text{-}Ce) \times V/M \quad (2)$$

3. Results and Discussion

3.1. Adsorbent properties.

Figure 1a displays the SEM analysis of nanoparticles, based on which it was determined that Fe_3O_4 nanoparticles coated with sodium dodecyl sulfate have a uniform and polished surface. The particles are small (around 51 nm), and they are spherical in shape.

Figures 2 b, c, and d signify the FTIR spectrum of Fe_3O_4/SDS and Fe_3O_4/SDS after the adsorption of catechol and p-cresol, respectively. Based on Figure 2b, it was determined that the adsorption peak observed at 545 cm^{-1} is related to the stretching vibrations of Fe_3O_4. In Figure 2c, the twin peak in the region of 3551 cm^{-1} is related to the hydrogen bond vibration lines of the phenolic O-H group, and the four adsorption peaks in the region of 1470 to 1622 cm^{-1} are related to the vibrations of the C=C ring, which indicates the aromatic structure of the benzene ring. At 1255 cm^{-1}, the vibrational bands of the C=O bond can be seen in the catechol. In Figure 2 d, in the region of 3500 cm^{-1}, the sharp peak is related to the vibrations of the phenolic group of cresol and the hydrogen bond, which is sharper than usual due to the existing aromatic group. The bands in the region of 2500 cm^{-1} are related to C-H stretching vibrations, and in the region between 1400 and 1600 cm^{-1}, C=C structural vibrations are visible, and the flux band at 1200 cm^{-1} shows the presence of C=O [31].

Magnetic features of Fe_3O_4/SDS were appraised by vibrating sample magnetometer (VSM) analysis (in the range of -10000 to 10000 Oe). The saturation magnetization value for Fe_3O_4/SDS nanocomposite was observed to be 28.1 emu/g (Figure 1e), which was fewer compared to the value reported for Fe_3O_4 in the articles (between 70 and 80 emu/g) [31, 32]. It approves the less ferromagnetic behavior for this nanocomposite compared to magnetic nanoparticles.

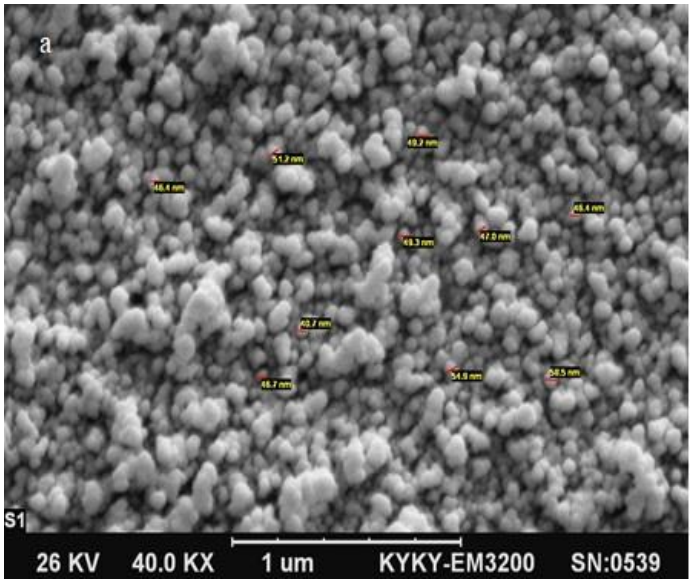

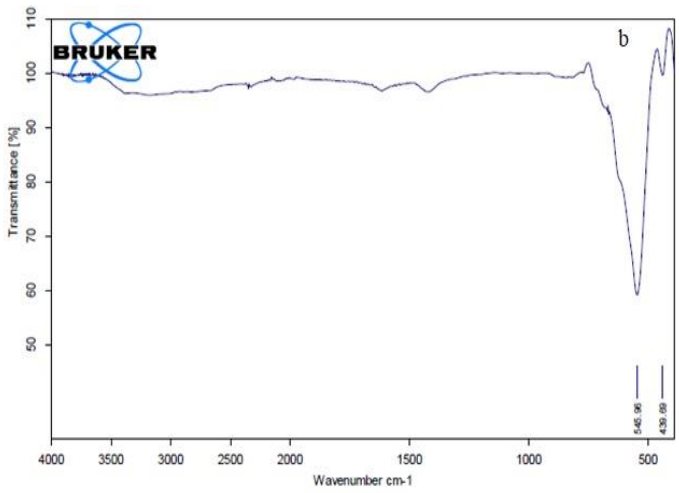

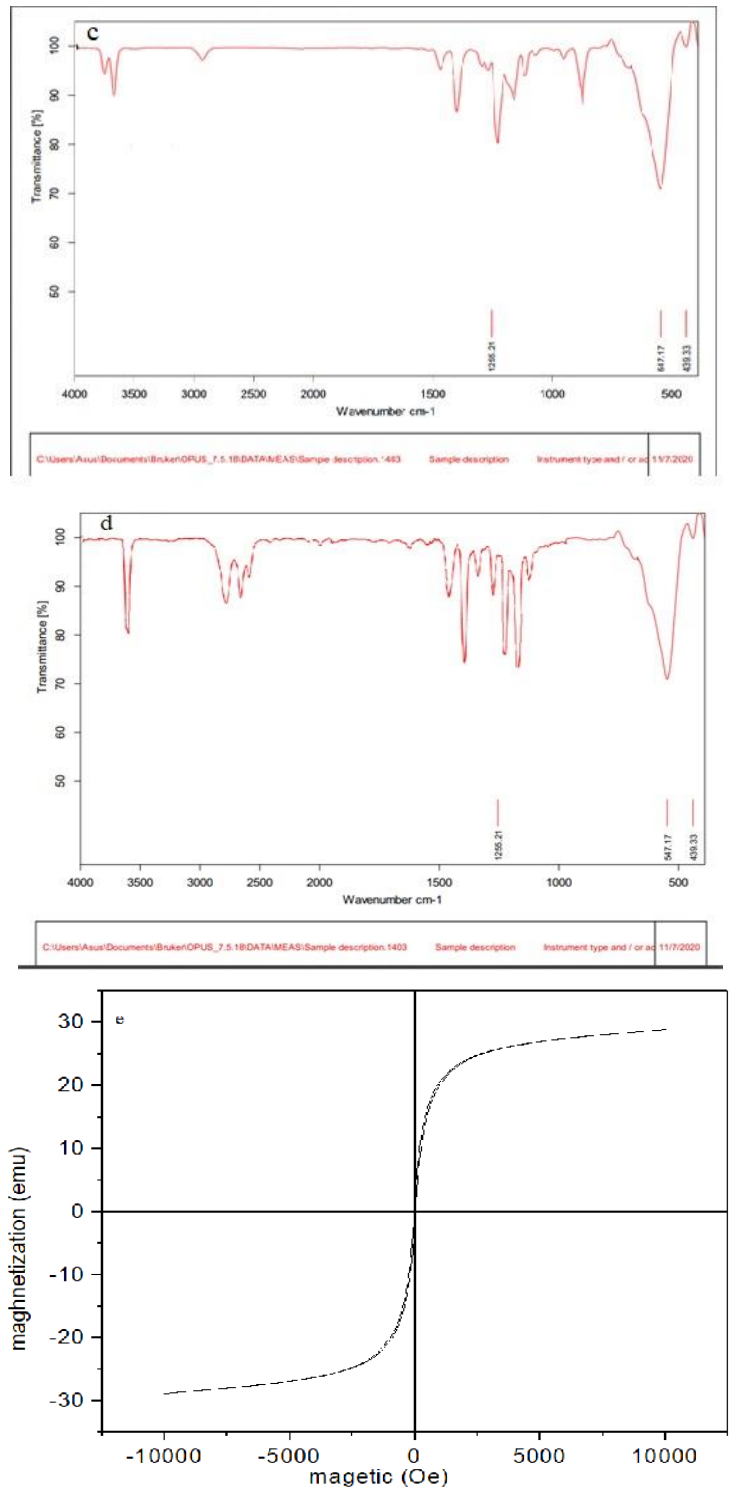

Figure 1. (**a**) SEM images of Fe_3O_4/SDS; (**b**) FTIR images of Fe_3O_4/SDS; (**c**) FTIR images of Fe_3O_4/SDS after catechol adsorption; (**d**) FTIR images of Fe_3O_4/SDS after p-cresol adsorption; (**e**) VSM images of Fe_3O_4/SDS.

3.2. Effect of parameters on the removal of p-cresol and catechol.

Due to the effect of pH on the adsorbent's surface charge and the solution's ionization charge, the solution pH is an implied factor on which the elimination of any substance depends. The effect of pH changes on adsorption by iron oxide magnetic nanoparticles was inspected in the pH range of 3-11. This pH range was chosen because when Fe_3O_4 dissolves at a pH less than 3, it causes the solution to darken. Also, at a pH higher than 11, magnetic nanoparticles move towards colloidal particles and do not exhibit any response to magnetic fields [37]. Figure

2a shows that the p-cresol removal efficiency by Fe_3O_4/SDS augmented from 60.2% to 91.2% for pH values from 3 to 7 and diminished from 91.2% to 84.4% with increasing pH from 7 to 11. Also, examination of Figure 2a shows that the removal efficiency of pyrocatechol by Fe_3O_4/SDS with increasing pH from 3 to 7 increased with a steep slope from 69.9% to 98.9%, and it then reduced with a slower slope from 98.9% to 90.7% with increasing pH from 7 to 11.

In the studies accomplished by Khalfa et al. [19] and Hu et al. [38], the findings were indicative of obtaining the highest removal efficiency at pH = 7. The reason for the adsorption of catechol on the adsorbent surface is the electrostatic force, and catechol is placed in the sites of the adsorbent surface through hydrogen bonding [16, 17]. The adsorption of catechol and p-cresol is based on their solubility and degree of ionization. Phenolic compounds are hardly dissolved in water, so that at low pH, they have a low degree of solubility and ionization, and their amount increases with increasing pH [1].

In order to determine pH_{PZC}, the solid addition method was used. The results are shown in Figure 2b. Considering the data obtained, it was determined that at pH = 6.1, the surface of the adsorbent has an electrical charge equal to zero. Therefore, the adsorbent surface will have a negative electrical charge for a pH above the zeta potential pH and a positive electrical charge at a pH lower than that. Also, when pH > pKa (pKa for catechol is 9.45 and for p-cresol is 9.8), catechol and p-cresol are negatively charged. However, the zeta potential of the isoelectric points of the adsorption sites also has a negative charge, which increases the force of electrostatic repulsion and prevents ions from spreading [28].

Examining Figure 3 shows for times from 10 to 30 min, the removal efficiency increases with a sharp slope at first, then increases with a slow slope from 30 to 60 min. The highest removal efficiency in the final graph is reached in 60 min, with a removal percentage of 91.2% and 98.9% for p-cresol and catechol, respectively. The removal of catechol and p-cresol is fast in the early stages due to empty active sites [39]. After a definite period of time, due to the saturation of the surface of the active adsorbent sites, the adsorption process reaches equilibrium, and the repulsive force prevents further removal [40].

Evaluation of Figure 4 shows that by raising the nanoparticle dose from 0.1 g/L to 0.4 g/L, the adsorption efficiency increases with a slow slope for both pollutants. It is detected to be constant for nanoparticle dose from 0.4 to 0.8 g/L. Therefore, the best removal efficiency is at the dose of 0.4 g/L, and the highest removal rate for p-cresol and pyrocatechol is 91.2% and 98.9%. By raising the amount of Fe_3O_4/SDS in the solution, the number of adsorption sites enhances, and therefore, the effective collision rate between the pollutant ions and the adsorbent increases [41]. The reason for the non-increase in the amount of adsorption with a greater rise in the amount of adsorbent can be linked to the overlapping of active sites on the surface of the adsorbent [42].

Examining Figure 5 displays that the removal efficiency for p-cresol and catechol develops with the increase of the initial concentration from 5 to 50 mg/L, and the removal efficiency decreases with the further increase of the initial concentration from 50 to 100 mg/L. Therefore, the best removal efficiency at 50 mg/L is 91.2% for p-cresol and 98.9% for catechol.

The removal efficiency is low at low concentrations until reaching the equilibrium concentration; this might be because, at low concentrations, the number of active adsorbent sites available for more pollutant ions is unreacted [43]. A tremendous increase in concentration leads to reduced removal efficiency of p-cresol. The reason is that with the increase of p-cresol and catechol ions, the amount of surface active sites of the adsorbent should also increase, but it is constant. Therefore, the number of ions is more than the active sites, and

the possibility of adsorption is less. As a result, the number of adsorbate ions will be higher than the available active sites for adsorption. The initial concentration as a reaction propellant is very important in the adsorption efficiency. With the concentration increase of the pollutant, the active adsorption sites are saturated, and the adsorption capacity decreases [44].

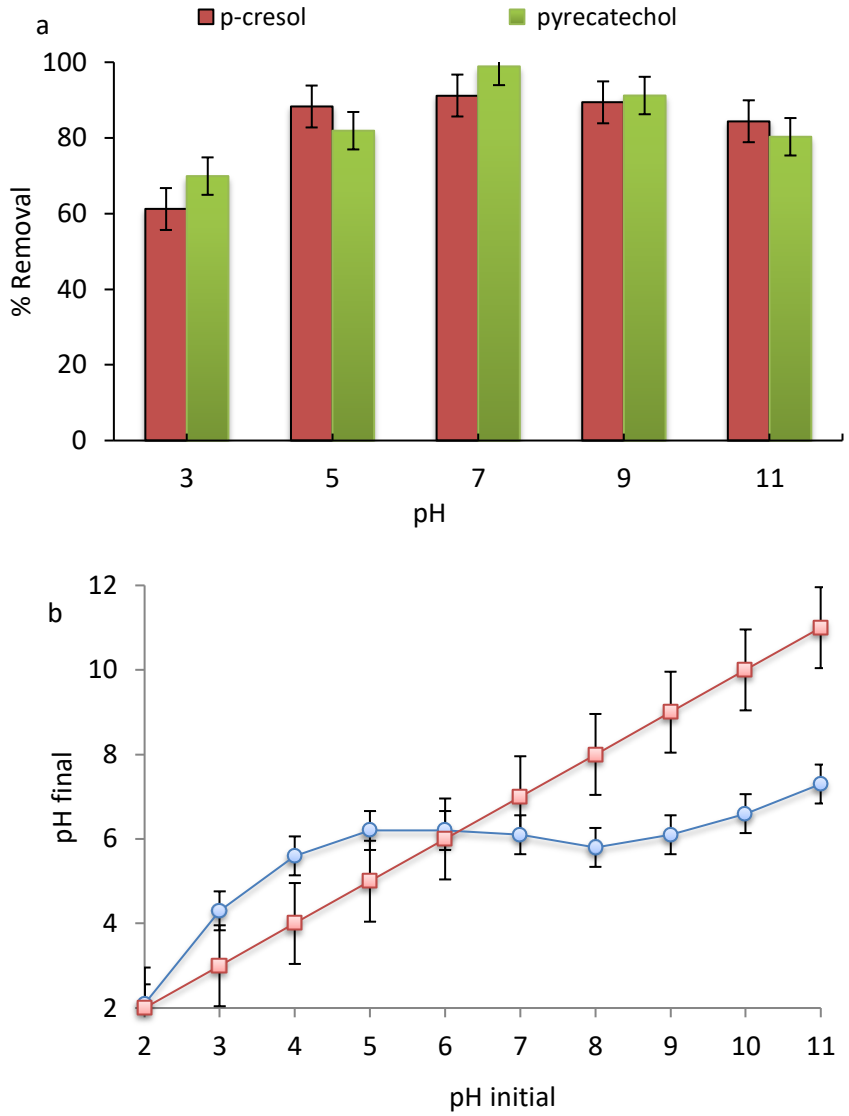

Figure 2. (**a**) Effect of pH on the adsorption of p-cresol and catechol by Fe_3O_4/SDS; (**b**) determine of point of zero charge; (Fe_3O_4/SDS dose: 0.4 g/L; temperature; 30 ℃: mixing time: 60 min and concentration: 50 mg/L).

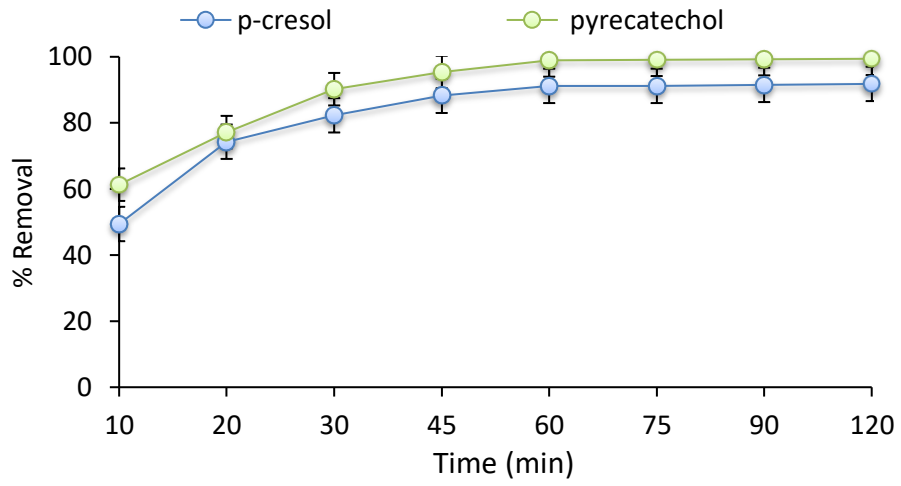

Figure 3. Effect of contact time on the adsorption of p-cresol and catechol By Fe_3O_4/SDS (Fe_3O_4/SDS dose: 0.4 g/L; temperature; 30 ℃: pH: 7 and concentration: 50 mg/L).

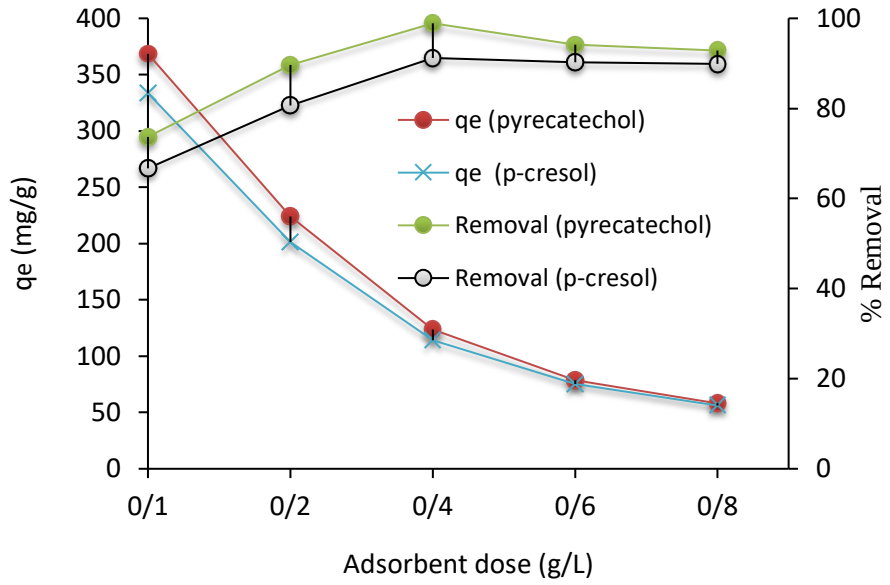

Figure 4. Effect of Fe_3O_4/SDS dose on the adsorption of p-cresol and catechol (time: 60 min; temperature; 30 ℃: pH: 7 and concentration: 50 mg/L).

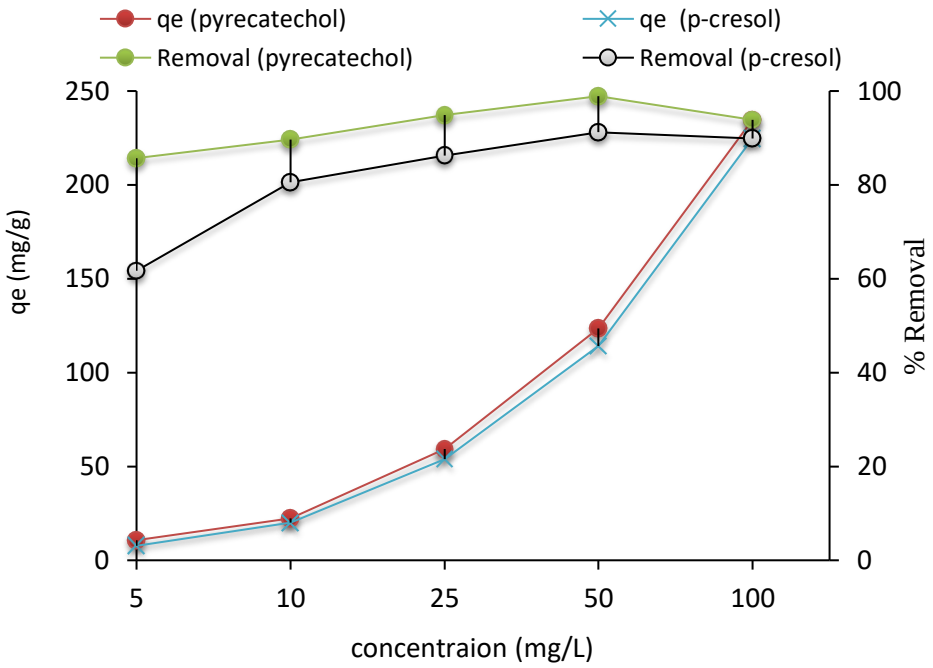

Figure 5. Effect of concentration on the adsorption of p-cresol and catechol (time: 60 min; temperature: 30 ℃: pH: 7 and Fe_3O_4/SDS dose: 0.4 g/L).

3.3. Effect of temperature and thermodynamics of adsorption.

Examining Figure 6 discloses that with the increase in temperature from 20 to 30° C, the removal efficiency increases with a steep slope. With a further rise in temperature from 30 to 40°C, the removal efficiency first increases with a very low slope and then decreases at 50°C. The final graph has a maximum peak at 40 °C with a removal efficiency of 91.2% and 98.9% for p-cresol and catechol, respectively.

Enhancing adsorption effectiveness with increasing temperature might also be described based on the chemical interaction between the adsorbate and adsorbent molecules

and the appearance of several new adsorption sites or the enhancement in the diffusion of pollutant molecules in the pores of the adsorbent [45]. After reaching an equilibrium reaction, a further increase in temperature weakens the binding force between the adsorbent and the adsorbate and thus reduces the process efficiency. In general, the increase in temperature due to the diminution in viscosity of the solution causes an increase in the diffusion of adsorbate molecules in the outer layer and internal pores of the adsorbent [46].

Further appraisal of the effectiveness of temperature on the p-cresol and pyrocatechol adsorption by Fe_3O_4/SDS was carried out based on thermodynamic parameters (i.e., ΔG^o, ΔH^o, and ΔS^o); these parameters are estimated using the thermodynamic formulas articulated by the below equations (3, 4, 5 and 6) [47]:

$$\Delta G° = -RT \ln K_C \quad (3)$$

$$K_C = \frac{C_{ads}}{C_e} \quad (4)$$

$$\ln K_C = \frac{\Delta S°}{R} - \frac{\Delta H°}{RT} \quad (5)$$

$$\Delta G° = \Delta H° - T\Delta S° \quad (6)$$

The intercept and the slope of the plot of (Ln Kc) against 1/T is the base for calculating values of ΔS^o and ΔH^o (Table 1). For negative ΔG^o values, a spontaneous adsorption process is expected. The positive ΔS^o represents the enhancement in randomness at the Fe_3O_4/SDS/p-cresol and pyrocatechol interface during the adsorption process. In addition, obtaining positive values for ΔH^o represents the endothermic nature of the adsorption of studied pollutants on the Fe_3O_4/SDS. ΔH^o values mostly offer a suggestion about the mechanism of adsorption; accordingly, the ΔH^o in the range of 0-20 kJ/mol is suggestive of physical adsorption, and the ΔH^o in the range of 80–200 kJ/mol represents chemisorption [48]. The low value of ΔH^o (35.6 and 41.2 kJ/mol for p-cresol and pyrocatechol, respectively) approves weak interaction between the p-cresol and pyrocatechol and Fe_3O_4/SDS and a more complex physicochemical process for adsorption [49].

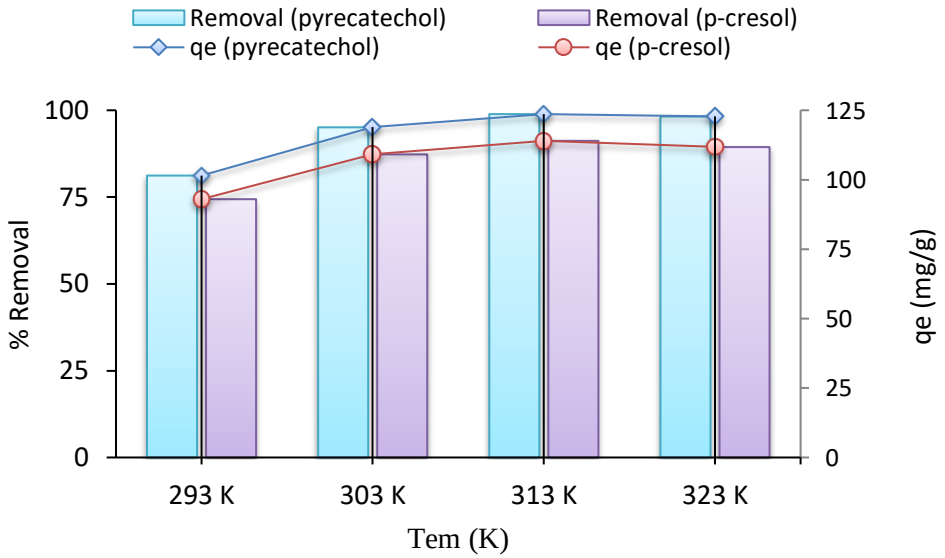

Figure 6. Effect of temperature on the adsorption of p-cresol and catechol (time: 60 min; concentration: 50 mg/L: pH: 7 and Fe_3O_4/SDS dose: 0.4 g/L).

Table 1. Thermodynamic parameters for the adsorption of p-cresol and catechol on Fe_3O_4/SDS.

T (K)	ΔG^0 (kJ/mol)	ΔH^0 (kJ/mol)	ΔS^0 (kJ/mol K)
p-cresol			
298	−0.851	35/6	0.0185

T (K)	ΔG^0 (kJ/mol)	ΔH^0 (kJ/mol)	ΔS^0 (kJ/mol K)
308	−1.62		
318	−3.27		
328	-3.14		
catechol			
298	−1.12		
308	−2.78		
318	−4.18	41/2	0/0198
328	-4.04		

3.4. Error functions.

This section of the study was conducted to assign the best-fitting isotherm and kinetic model; to attain the purpose of this section, four creditable error functions were employed to count the error deviation between experimental and predicted equilibrium adsorption data after utilizing both linear and nonlinear models. The assumption considered for utilizing the error methods was that both the liquid phase concentration and the solid phase concentration contribute equally to weighting the error criterion for the model solution procedure. Table 2 represents equations related to the error functions [50].

3.5. Determination of adsorption kinetics.

The kinetics study is necessary to investigate the factors affecting the reaction rate and show the pollutant adsorption process with time. Accordingly, contact times between 10 and 120 min were considered to conduct the p-cresol and pyrocatechol adsorption experiments on Fe3O4/SDS and elucidate their sorption mechanism. For target experiments, optimum values of other studied parameters were applied. Kinetic models employed for investigating the sorption mechanisms in the present study were the nonlinear and linear PFO, PSO, Elovich, and IPD models; the equations of these models are represented in Table 3. In Figures 7a and b, the nonlinear plots were brought, and the achieved values of all parameters were represented in Table 3. According to our observations, the most appropriate models for describing the adsorption of p-cresol and pyrocatechol on the Fe_3O_4/SDS might be the linear kinetic models of PFO, PSO, and Elovich since the coefficients of determination were observed to be closer to unity (R^2> 0.95). Nevertheless, error functions obtained from the PSO model had a low value, which indicates this kinetic model's potential for unfolding the adsorption of p-cresol and pyrocatechol. According to the PFO kinetic model results, p-cresol and pyrocatechol molecules were rapidly binding to the surface of Fe_3O_4/SDS, and then equilibrium was obtained. Experimental results related to adsorption capacity for PSO kinetics were observed to be close to amounts adsorbed at equilibrium.

In the present study, IDP mechanisms were also used to analyze the data to obtain more information about the adsorption mechanism. Exploring the possibility of IPD was studied by applying the IPD model (Weber–Morris model) to the present work data. C, an arbitrary constant, symbolizes the boundary layer thickness; a larger C value is indicative of a thicker boundary layer. For C=0, there is no boundary layer, and passing through a linear line from the origin is expected. Therefore, film diffusion (due to no or less thickness) could be ignored; hence, IPD would be considered the rate-controlling step during the entire adsorption kinetic process [51]. Nevertheless, above mentioned explanations were only the theoretical explanation for the employment of the IPD Equation. Many studies have reported nonzero intercepts, indicating that IPD and film diffusion are rate-limiting steps in most adsorption processes. Considering Figure 7c and Table 3, since there is a very low R^2 with the single

regression line for IPD, it cannot anticipate one linear line for the experimental data. Instead, IPD can be split into two or three different parts with linear regressions for all cases, as shown in Figure 7c, illustrating the film's and IPD in controlling the adsorption diffusion. In another study, three regressions in different pores sizes (macro, meso, and micro) with a horizontal line as the equilibrium have been reported for IPD diffusion. Another study reported three linear regions (i.e., initial quick loading on surface, pore diffusion, and final horizontal equilibrium); nevertheless, differentiation of these three or four regions in this study was not easy. Accordingly, the detection of two linear regions was primarily reported so that the adsorption process between the film and IPD could elucidate it. As well, the film diffusion could represent the initial rapid increase.

3.6. Adsorption isotherm.

Adsorption isotherms are equilibrium data employed for describing the reaction between the adsorbate and the adsorbent. They also put into words the adsorption capacity of an adsorbent [38]. This study utilized four isotherm models to scrutinize the experimental data and designate the equilibrium state. This study also utilized the nonlinear analysis; its employment is to evade errors raised by different estimates resulting from simple linear regression of the linearized forms of the isotherm equations (represented in Table 4). These errors can affect R2 values significantly.

The Langmuir model indicates the single-layer and uniform (homogeneous) adsorption of the studied pollutants with the same energy on all surfaces of the adsorbent and also states that all the adsorption sites had the same continuity with respect to the evaluated pollutant molecules. The experimental equation of the Freundlich isotherm is based on the multi-layer, non-uniform, and heterogeneous adsorption of the adsorbate on the adsorbent [39, 40].

The D-R isotherm is a model which is ordinarily utilized for evaluating the mechanisms of adsorption on porous and heterogeneous surfaces. It is a temperature-dependent model that determines physical or chemical adsorption's characteristic porosity and free energy [52].

Using Temkin isotherm, the effects of interactions between adsorbent-adsorbate molecules on the adsorption are indirectly examined. The supposition of mentioned isotherm is that the adsorption heat of whole molecules drops linearly (not logarithmically) in systems where extremely high or low concentrations are neglected [53].

The equations related to the isotherms are presented in Table 4. As shown, the regression coefficient is high for Langmuir isotherm, and the error coefficients are lower for both materials. Moreover, the operational adsorption capacity value is almost equal to the calculated adsorption capacity.

According to Freundlich isotherm, the favorable adsorption process occurs when the values of "n" are between 1 and 10. According to Table 4, "n" values were between 1 and 10, which embodies the superiority of the adsorption process. Also, examination of the R2 and error coefficient values exhibited the conformation of adsorption to the Langmuir isotherm as well as a monolayer adsorbent surface and homogeneous pore distribution.

Based on calculations, the values of E were observed to be in the range of 1.00 to 5.00 kJ/mol (Table 4); based on this, the adsorption process would proceed physically since E values are <8 kJ/mol. Moreover, the values of Qm were detected to be relatively lower compared to qm observed for the Langmuir isotherm.

Temkin isotherm was another model employed in this study for investigating the interactions between adsorbent and adsorbate; this was done by applying the raw data to this

model. The *b* for p-cresol and pyrocatechol were 11.2, 19.1, 24.3, and 29.1 J/mol for linear and nonlinear, respectively; this confirms the presence of simultaneous physical and chemical adsorption in this process. In addition, examining the R2 values showed the order of applicability of studied isotherms below: Langmuir > Temkin > Freundlich > D-R.

Table 2. Errors functions and their equations.

Error function	Abbreviation	Formula	References
Residual Root Mean Square Error	RMSE	$\sqrt{(\frac{1}{n-1}\sum_{i=1}^{n}(q_{e,exp}-q_{e,cal}))^2}$	[39]
Average Relative Error	ARE	$\frac{100}{n}\sum_{i=1}^{n}\left\|\frac{q_{e,exp}-q_{e,cal}}{q_{e,exp}}\right\|_i$	[40]
Sun of absolute errors	EABS	$\sum_{i=1}^{n}\left\|q_{e,exp,i}-q_{e,cal,i}\right\|$	[41]
Non linéaire chi-square test	χ^2	$\sum_{i=1}^{n}\frac{(q_{e,cal}-q_{e,exp})^2}{q_{e,exp}}$	[42]

Table 3. Kinetic parameters for the adsorption of p-cresol and pyrocatechol adsorption onto the Fe_3O_4/SDS.

Model	Parameters	Linear	Nonlinear	Linear	Nonlinear
Qe exp	------	147.1	139.6	159.1	152.3
PFO $Log\ (q_e - q_t) = \log q_e - \frac{K_1}{2.303}t$ [51] q_e = adsorption capacity at equilibrium time and q_t = adsorption capacity at time t (mg/g), K_1 (1/min) = equilibrium rate constant for PFO	$q_{e\ (cal)}$	127.1	112.3	127.1	120.2
	K_1	0.027	0.036	0.034	0.043
	R^2	0.936	0.832	0.911	0.842
	X^2	7.25	8.72	6.41	8.11
	HYBRID	8.24	8.53	5.27	9.16
	ARE	6.98	7.24	6.44	9.44
	MPSD	5.64	5.47	7.11	5.44
PSO $\frac{t}{q_t} = \frac{1}{K_2 q_e^2} + \frac{t}{q_e}$ [54] K_2 (g/mg. min)= equilibrium rate constant for PSO	$q_{e\ (cal)}$	143.2	147.1	156.1	152.3
	K_2	0.0027	0.0044	0.0035	0.0029
	R^2	0.998	0.912	0.991	0.902
	X^2	1.07	1.43	0.921	1.14
	HYBRID	0.933	1.23	1.15	0.765
	ARE	0.921	0.568	1.08	1.72
	MPSD	0.944	1.84	1.49	1.56
Elovich $q_t = \frac{1}{\beta}\ell n(\alpha\beta) + \frac{1}{\beta}\ell n(t)$ [55] q_t= amount of adsorbate/g adsorbent at time (t), α is the initial adsorption rate (mg/g-min); β is the desorption constant (g/mg) during any one experiment.	$\alpha\times10^6$	11.2	17.4	11.8	9.71
	β	0.0044	0.0053	0.0064	0.0072
	R^2	0.895	0.823	0.924	0.902
	X^2	3.21	3.27	5.14	4.16
	HYBRID	6.16	7.11	4.05	7.26
	ARE	9.19	5.23	7.86	9.35
	MPSD	3.17	4.34	8.44	8.29
IPD $q_t = K_b\ t^{1/2} + C$ [56] K_b =IPD rate constant (mg/g. $min^{1/2}$) C= thickness of the boundary layer	Stage 1				
	K_b	11.9		12.4	
	C	1.94		2.24	
	R^2	0.951		0.965	
	Stage 2				
	K_b	3.14		4.45	
	C	4.35		7.19	
	R^2	0.973		0.912	
	Stage 3				
	K_b	0.047		0.245	
	C	18.1		23.1	
	R^2	0.916		0.943	

Also, the nonlinear results of the isotherms are portrayed in Figure 8a-b and Table 4. As can be seen, the Langmuir isotherm model has the best fit with equilibrium data due to its

high regression coefficient and lower error coefficient. Also, the nonlinear diagram of the Langmuir isotherm is more consistent with the equilibrium diagram shown in Figure 8a-b. Table 5 compares the adsorption capacities of different adsorbents for removing p-cresol and pyrocatechol with our studied adsorbent.

Table 4. The parameters of the isotherms for p-cresol and pyrocatechol adsorption onto the Fe_3O_4/SDS.

Models	Parameters	p-cresol		pyrocatechol	
		Linear	nonlinear	Linear	nonlinear
		293 K	303	313	323
Langmuir $\frac{1}{Q_e}=\frac{1}{Q_{max}}+\frac{1}{Q_{max}K_L Ce}$, $R_L=\frac{1}{1+K_L C_o}$ K_L=Langmuir isotherm constant (L/mg). Q_{max}=maximum monolayer coverage capacity (mg/g).	Q_{max}	161.2	157.3	174.2	173.8
	K_L	0.027	0.041	0.072	0.051
	R^2	0.979	0.989	0.993	0.983
	R_L	0.27	0.196	0.121	0.163
	HYBRID	1.17	1.29	1.42	1.76
	RMSE	2.35	1.52	2.07	1.29
	ARE	1.17	2.53	1.52	2.17
	X^2	2.41	2.13	2.17	1.69
Freundlich $\log Q_e=\log K_F+\frac{1}{n}\log C_e Q_e$ capacity adsorption (mg/g); K_F Freundlich indicator of adsorption capacity (mg/g)/(mg/L)^n ,1/n_F Intensity of the adsorption indicating the surface heterogeneity and favorability of the adsorption process.	K_F	0.07	0.053	0.112	0.127
	1/n	0.212	0.273	0.311	0.327
	R^2	0.972	0.946	0.919	0.923
	HYBRID	3.17	6.25	7.19	10.2
	RMSE	3.26	5.14	7.13	4.29
	ARE	6.25	4.19	8.71	5.26
	X^2	11.2	9.81	8.29	6.34
Temkin $Q_e=\frac{RT}{b}\ln A_T+\frac{RT}{b}\ln C_e$ b =Temkin isotherm constant related to the heat of adsorption J/mol and A_T is the Temkin isotherm equilibrium binding constant (L/g). R= universal gas constant (8.314 J/mol/K). T= absolute Temperature in Kelvin	b	11.2	19.1	24.3	29.1
	A_T	71.2	65.4	39.2	52.3
	R^2	0.893	0.923	0.946	0.952
	B	43.3	37.5	31.6	29.9
	HYBRID	6.17	8.25	4.23	5.62
	RMSE	6.43	8.53	9.56	8.11
	ARE	10.2	11.3	7.35	8.44
	X^2	6.27	11.2	8.14	7.29
D-R $\ln q_e=\ln q_m-B\varepsilon^2$, $E=\frac{1}{2B^{0.5}}$ $\varepsilon=RT\ell n\left[1+\frac{1}{C_e}\right]$ Q_m= theoretical adsorption isotherm saturation capacity (mg/g). B is the D-R isotherm constant (mol^2/kJ^2), ε is Polanyi potential. E= average energy of adsorption kJ/mol	Q_m	78.1	93.2	108.3	112.2
	R^2	0.931	0.872	0.973	0.879
	E	4.75	3.87	3.42	2.21
	HYBRID	5.16	8.21	5.12	7.21
	RMSE	5.19	7.83	6.45	6.83
	ARE	6.53	6.23	3.71	7.23
	X^2	4.04	5.71	5.89	4.47

Table 5. Comparison of adsorption capacity of different adsorbents.

Adsorbent	Pollutant	Q_m (mg g^{-1})	Reference
activated sludge	p-cresol	51.2	[6]
hydroxyapatite	p-cresol	44.6	[9]
activated charcoal	p-cresol	39.2	[12]
coconut shell-AC	p-cresol	40.3	[13]
MWCNTs	catechol	71.4	[17]
Graphene oxide	catechol	53.5	[18]
Dolomite	catechol	52.3	[19]
MWCNT	p-cresol	64.4	[20]
Granular AC	p-cresol	35.6	[22]
Al_2O_3- MWCNT	p-cresol	41.5	[23]
AC-Sunflower	catechol	62.8	[25]
Fe_3O_4/SDS	p-cresol	161.2	This study
Fe_3O_4/SDS	catechol	174.2	This study

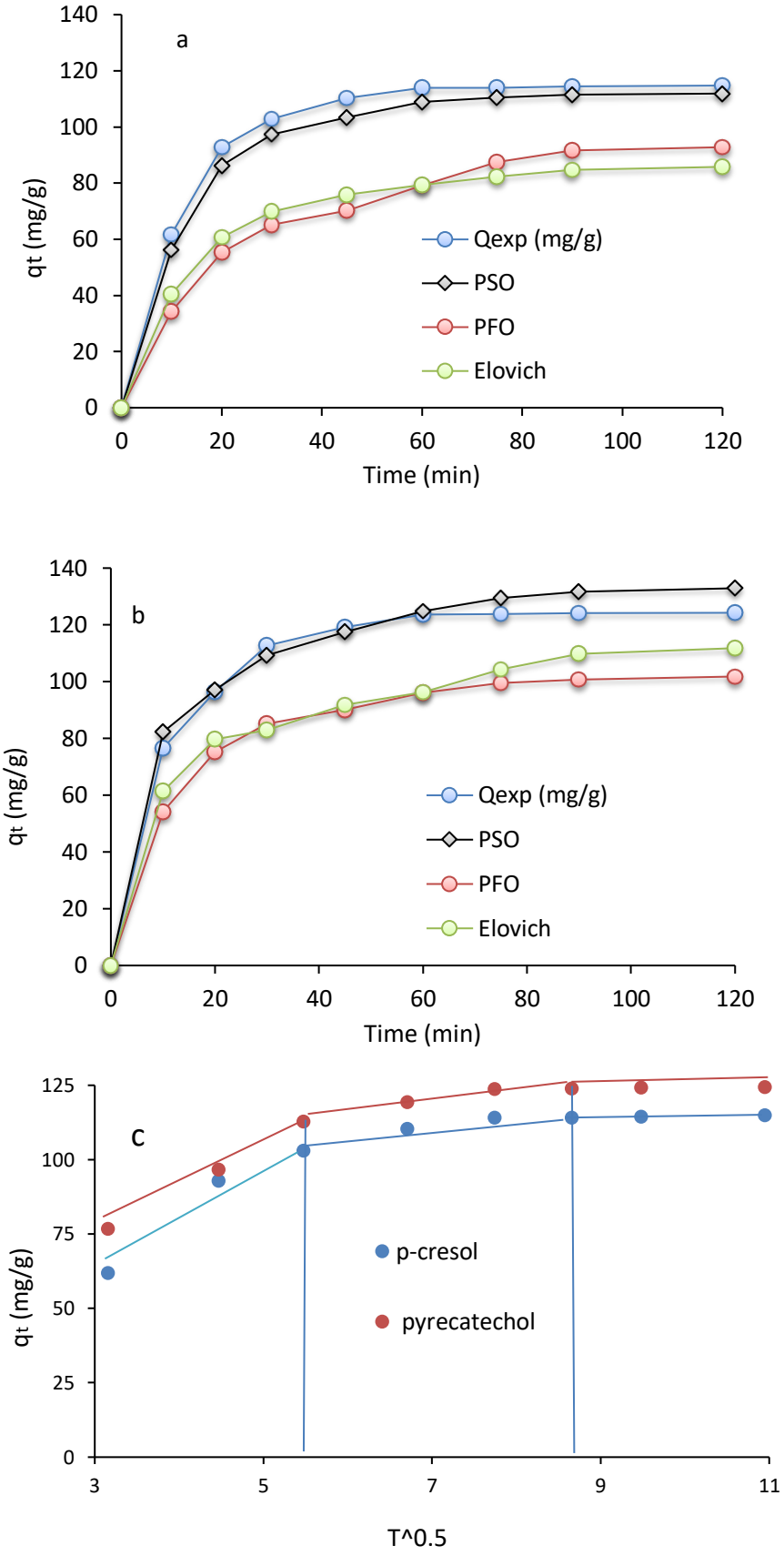

Figure 7. (**a**) Nonlinear kinetic plot for p-cresol adsorption; (**b**) Nonlinear kinetic plot for pyrocatechol adsorption; (**c**) IPD plot for p-cresol and pyrocatechol adsorption.

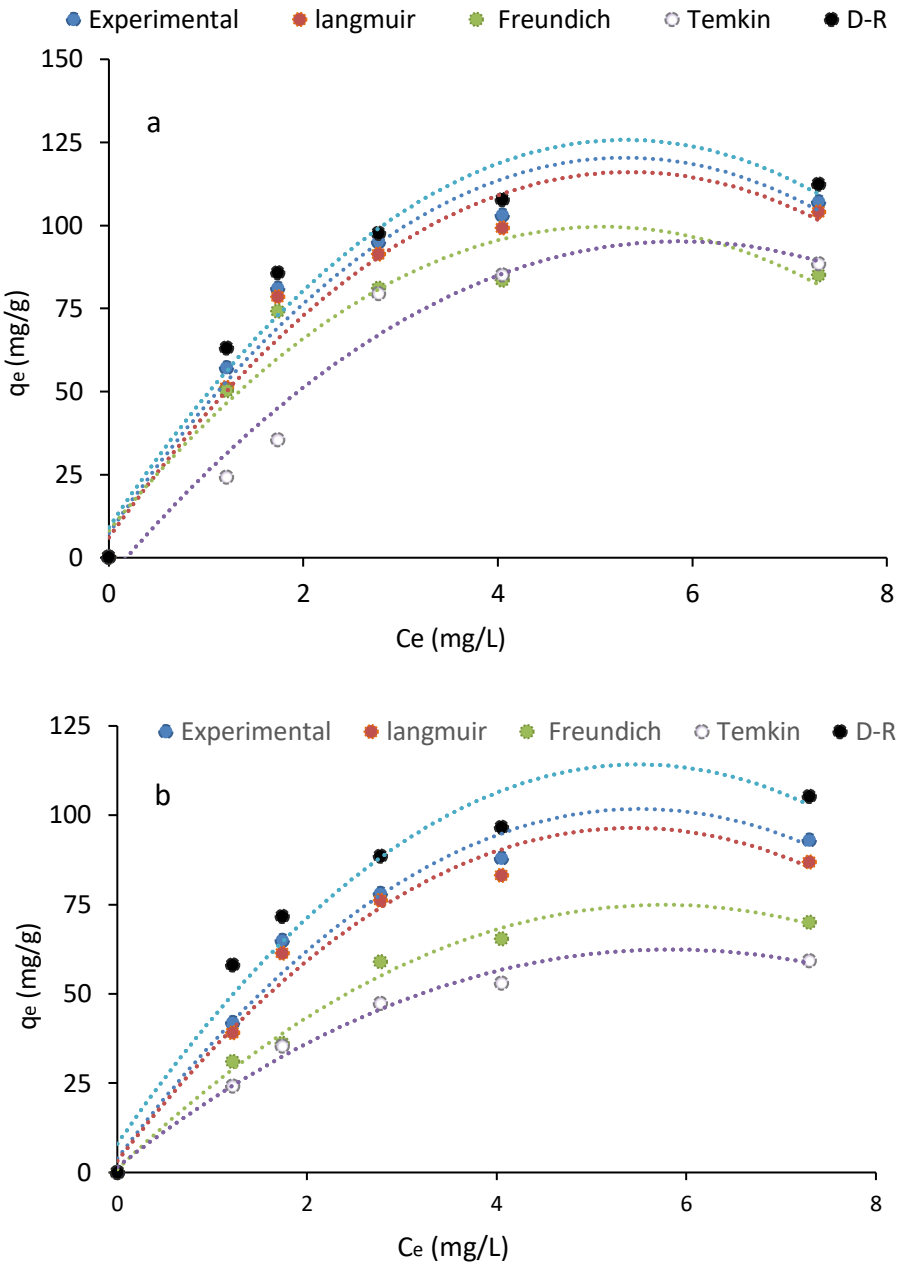

Figure 8. (**a**) Nonlinear isotherm plot for pyrocatechol adsorption; (**b**) Nonlinear kinetic plot for p-cresol adsorption.

3.7. Desorption and reuse.

One of the most important parts of a treatment process with conventional methods, which is very important from the economic and environmental point of view, is the adsorbent recovery and its reuse. In this study, adsorption-desorption was accomplished using methanol; three stages of adsorption-desorption were carried out consecutively, and the results are depicted in Figure 9. As observed, for both p-cresol and pyrocatechol, a very small change in adsorption was observed after three adsorption and desorption stages. This gradual decrease is also normal, because, in each desorption stage, a small amount of adsorbent is lost. In a study performed by Al-Musawi et al. for the recovery of magnetic chitosan, about an 8 percent reduction in efficiency in removing Acid Blue 113 dye was observed after six steps; the reason for this is the reduction of the adsorbent during the washing step (32).

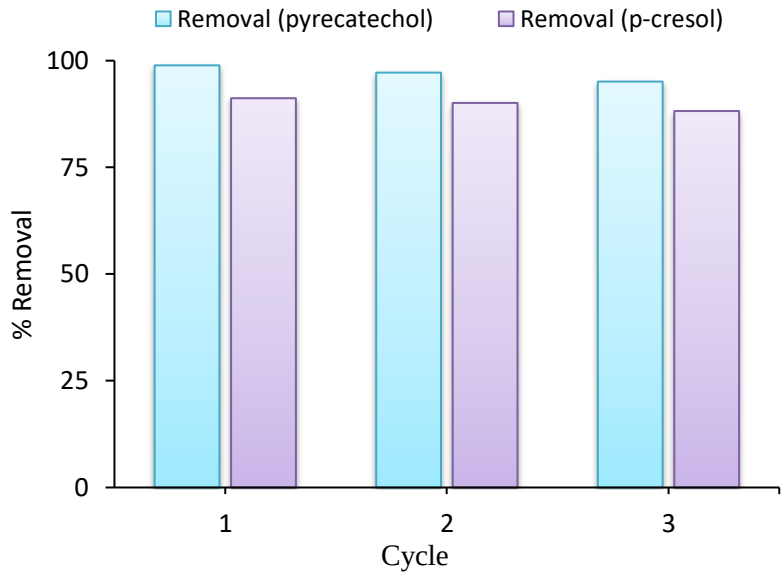

Figure 8. Recycling and reuse of adsorbent to remove p-cresol and pyrocatechol.

4. Conclusions

In this study, the removal efficiency of pyrocatechol and p-cresol was measured by Fe_3O_4/SDS under optimal conditions, and its value was 98.9% for pyrocatechol and 91.2% for p-cresol. In this study, the effect of different parameters showed that neutral pH and contact time of 60 minutes at a concentration of 50 mg/L had the maximum elimination efficiency for p-cresol and pyrocatechol. Due to the high regression and lower error coefficients, Langmuir isotherm and PSO kinetics had the best agreement with equilibrium data. Therefore, Fe_3O_4/SDS is an adsorbent with very high ability and is economically suitable for removing various pollutants from aqueous solutions.

Funding

This research received no external funding.

Acknowledgments

The authors are grateful to the Zahedan University of Medical Sciences for the financial support of this study (project code: 9507).

Conflicts of Interest

The authors declare no conflict of interest.

References

1. Diyanati, R.A.; Yousefi, Z.; Cherati, J.Y.; Investigating phenol adsorption from aqueous solution by dried azolla. *J Mazand Uni of Med Sci*. **2013**, *22*; 13-21.
2. Al-Musawi, T.J.; Mengelizadeh, N.; Ganji, F.; Wang, C. Preparation of multi-walled carbon nanotubes coated with $CoFe_2O_4$ nanoparticles and their adsorption performance for Bisphenol A compound. *Adv. Powder Technol*. **2022**, *33*,103438, https://doi.org/10.1016/j.apt.2022.103438
3. Balarak, D.; Mostafapour, F.K.; Lee, S.M.; Jeon, C. Adsorption of bisphenol A using dried rice husk: Equilibrium, kinetic and thermodynamic studies. *Appl. Chem. Eng* **2019**, *30*, 316-323, http://www.koreascience.or.kr/article/JAKO201917970705709.page.

4. Balarak, D.; Joghataei, A. Biosorption of Phenol using dried Rice husk biomass: Kinetic and equilibrium studies. *Pharm Chem*. **2016**; *8*, 96-103, https://koreascience.kr/article/JAKO201917970705709.page.
5. Diyanati, R.; Yazdani, J.; Belarak, D. EEffect of sorbitol on phenol removal rate by lemna minor. *J Mazand Uni of Med Sci*. **2013**; *22*, 58-65, http://jmums.mazums.ac.ir/article-1-2030-en.html.
6. Xenofontos, E.; Tanase, A-M.; Stoica, I.; Vyrides, I. Newly isolated alkalophilic Advenella species bioaugmented in activated sludge for high p-cresol removal. *New Biotechnol*. **2016**, *33*, 305-10, https://doi.org/10.1016/j.nbt.2015.11.003.
7. Usha, S.P.; Gupta, B.D.; Urinary p-cresol diagnosis using nanocomposite of ZnO/MoS_2 and molecular imprinted polymer on optical fiber based lossy mode resonance sensor. *Biosens. Bioelectron*. **2018**, *101*, 135-45, https://doi.org/10.1016/j.bios.2017.10.029
8. Mahdavianpour, M.; Moussavi, G.; Farrokhi, M. Biodegradation and COD removal of p-Cresol in a denitrification baffled reactor: Performance evaluation and microbial community. *Process Biochem*. **2018**, *69*, 153-60. https://doi.org/10.1016/j.procbio.2018.03.016.
9. Ooi, C.H.; Ling, Y.P.; Pung, S.Y.; Yeoh, F.Y. Mesoporous hydroxyapatite derived from surfactant-templating system for p-Cresol adsorption: Physicochemical properties, formation process and adsorption performance. *Powder Technol*. **2019**, *342*, 725-34, https://doi.org/10.1016/j.powtec.2018.10.043.
10. Silva, C.; Gómez, J.; Beristain-Cardoso, R. Simultaneous removal of 2-chlorophenol, phenol, p-cresol and p-hydroxybenzaldehyde under nitrifying conditions: kinetic study. *Bioresour. Technol*. **2011**, *102*, 6464-8, https://doi.org/10.1016/j.biortech.2011.03.105.
11. Suresh, S.; Srivastava, V.C.; Mishra, I.M. Adsorption of catechol, resorcinol, hydroquinone, and their derivatives: a review. Inter. *J. Energy and Environ. Eng*. **2012**, *3*, 1-19, https://d-nb.info/1094688827/34.
12. Bakas, I.; Elatmani, K.; Qourzal, S.; Barka, N.; Assabbane, A.; Aît-Ichou, I. A comparative adsorption for the removal of p-cresol from aqueous solution onto granular activated charcoal and granular activated alumina. *J Mater Environ Sci*. **2014** *5*, 675-82.
13. Zhu, Y.; Kolar, P. Investigation of adsorption of p-cresol on coconut shell-derived activated carbon. *J. Taiwan Ins. Chem. Eng*. **2016**, *68*, 138-46, https://doi.org/10.1016/j.jtice.2016.07.044.
14. Diyanati, R.A.; Yousefi, Z.; Cherati, J.Y. The ability of Azolla and lemna minor biomass for adsorption of phenol from aqueous solutions. *J. Mazand. Uni. Med. Sci*. **2013**, *23*,17-23, http://jmums.mazums.ac.ir/article-1-2360-en.html.
15. Tušek, A.J.; Šalić, A.; Zelić, B. Catechol removal from aqueous media using laccase immobilized in different macro-and microreactor systems. *Appl. Biochem. Biotechnol*. **2017**, *182*, 1575-90, https://link.springer.com/article/10.1007/s12010-017-2419-2.
16. Kermani, M.; Farzadkia, M.; Esrafili, A.; Jokandan, S.F.; Badi, M.Y. Removal of catechol from aqueous solutions using catalytic ozonation by magnetic nanoparticles of iron oxide doped with silica and titanium dioxide: a kinetic study. *J. Mazand. Uni. Med. Sci*. **2016**, *26*, 139-54.
17. Ahmadi, S.; Shadman, M.; Hossini, H.; Hashemi, S. Catechol removal using MWCNTs from synthetic solutions: modeling, equilibrium and kinetics. *J. Mater. Environ. Sci*. **2016**, *7*, 3885-94, https://www.jmaterenvironsci.com/Document/vol7/vol7_N10/417-JMES-2495-Ahmadi.pdf.
18. Tazerodi, A.J.; Akbari, H.; Mostafapour, F. Adsorption of catechol from aqueous solutions using graphene oxide. *J. Human, Environ. Health Prom*. **2018**, *4*, 175-9, https://stu-cul.zums.ac.ir/jhehp/article-1-190-en.html.
19. Khalfa, A.; Mellouk, S.; Marouf-Khelifa, K.; Khelifa, A. Removal of catechol from water by modified dolomite: performance, spectroscopy, and mechanism. *Water Sci. Technol*. **2018**, *77*, 1920-30, https://doi.org/10.2166/wst.2018.071.
20. Hu, F.; Chen, S.; Wang, C.; Yuan, R.; Yuan, D.; Wang, C. Study on the application of reduced graphene oxide and multiwall carbon nanotubes hybrid materials for simultaneous determination of catechol, hydroquinone, p-cresol and nitrite. *Anal. Chim. Acta*. **2012**, *724*, 40-6, https://doi.org/10.1016/j.aca.2012.02.037.
21. Ma, D.Y.; Zhang, S.Y.; Zhan, S.H.; Feng, L.T.; Zeng, S.G.; Lin, Q-Q. Adsorptive Removal of Catechol from Aqueous Solution with a Water-Stable and Hydroxyl-Functionalized Terbium–Organic Framework. *Ind. Eng. Chem. Res*. **2019**, *58*, 20090-8, https://doi.org/10.1021/acs.iecr.9b05067.
22. Das, L.; Kolar, P.; Osborne, J.; Classen, J. Adsorption of p-cresol on granular activated carbon. Agricultural Engineering International: *CIGR J*. **2012**, *14*, 37-49, https://cigrjournal.org/index.php/Ejounral/article/view/2171.
23. Jaafari, J.; Ghozikali, M.G.; Azari, A.; Delkhosh, M.B.; Javid, A.B.; Mohammadi, AA. Adsorption of p-Cresol on Al_2O_3 coated multi-walled carbon nanotubes: response surface methodology and isotherm study. *J. Ind. Eng. Chem*. **2018**, *57*, 396-404, https://doi.org/10.1016/j.jiec.2017.08.048.
24. Garba, Z.N.; Rahim, A.A. Evaluation of optimal activated carbon from an agricultural waste for the removal of para-chlorophenol and 2, 4-dichlorophenol. *Process safe. Environ. Prot.* **2016**, *102*, 54-63, https://doi.org/10.1016/j.psep.2016.02.006.
25. Houndedjihou, D.; MonjereziV M.; Muleja, A.A.; Kodom, B. Adsorption, kinetics and equilibrium studies on removal of catechol and resorcinol from aqueous solution using low-cost activated carbon prepared from

sunflower (Helianthus annuus) seed hull residues. *Water, Air, & Soil Pollution*. **2018**, *229*, 1-23, https://link.springer.com/article/10.1007/s11270-018-3993-9.
26. Sen, B.K.; Deshmukh, D.K.; Deb, M.K.; Verma, D.; Pal, J. Removal of phenolic compounds from aqueous phase by adsorption onto polymer supported iron nanoparticles. *Bull. Environ. Contam. Toxico*l. **2014**, *93*, 549-54, https://link.springer.com/article/10.1007/s00128-014-1381-8.
27. Al-Musawi, T.J.; McKay, G.; Kadhim, A. Activated carbon prepared from hazelnut shell waste and magnetized by Fe_3O_4 nanoparticles for highly efficient adsorption of fluoride. *Biomass Conv. Bioref*. **2022**, *12*, 1-11. https://doi.org/10.1007/s13399-022-02593-z.
28. Mahvi, A.H.; Balarak, D.; Bazrafshan, E. Remarkable reusability of magnetic Fe_3O_4-graphene oxide composite: a highly effective adsorbent for Cr(VI) ions. *Int. J. Environ. Anal. Chem.* **2021**, *100*, 1-11, https://doi.org/10.1080/03067319.2021.1910250.
29. Rajiv, P.; Mengelizadeh, N.; McKay, G. Photocatalytic degradation of ciprofloxacin with Fe_2O_3 nanoparticles loaded on graphitic carbon nitride: mineralisation, degradation mechanism and toxicity assessment. *Int. J. Environ. Anal. Chem*. **2021**, *100*, 1-11, https://doi.org/10.1080/03067319.2021.1890059
30. Al-Musawi, T.J., Mahvi, A.H., Khatibi, A.D. Effective adsorption of ciprofloxacin antibiotic using powdered activated carbon magnetized by iron(III) oxide magnetic nanoparticles. *J Porous Mater*. **2011**, *28*, 835–852, https://doi.org/10.1007/s10934-021-01039-7.
31. Yilmaz, M., Al-Musawi, T.J., Saloot, M.k. Synthesis of activated carbon from Lemna minor plant and magnetized with iron (III) oxide magnetic nanoparticles and its application in removal of Ciprofloxacin. *Biomass Conv. Bioref*. **2022**, *12*, 1-11, https://doi.org/10.1007/s13399-021-02279-y.
32. Al-Musawi, T.J.; Mengelizadeh, N.; Al Rawi, O. Capacity and Modeling of Acid Blue 113 Dye Adsorption onto Chitosan Magnetized by Fe_2O_3 Nanoparticles. *J Polym Environ*. **2022**, *30*, 344–359, https://doi.org/10.1007/s10924-021-02200-8.
33. Abedi, M.; Ahmadmoazzam, M.; Jaafarzadeh, N. Removal of cationic tolonium chloride dye using Fe_3O_4 nanoparticles modified with sodium dodecyl sulfate. *Chem. Biochem. Eng. Q*. **2018**, *32*, 205-13, https://hrcak.srce.hr/file/299090.
34. Shariati, S.; Faraji, M.; Yamini, Y.; Rajabi, A.A. Fe_3O_4 magnetic nanoparticles modified with sodium dodecyl sulfate for removal of safranin O dye from aqueous solutions. *Desalination* **2011**, *270*, 160-5, https://doi.org/10.1016/j.desal.2010.11.040.
35. Kanthasamy, S.; Hadibarata, T.; Hidayat, T.; Alamri, S.A.; Ahmed al-Ghamdi, A. Adsorption of azo and anthraquinone dye by using watermelon peel powder and corn peel powder: Equilibrium and kinetic studies. *Biointerface Res. Appl. Chem*. **2020**, *10*, 4706–4713, https://doi.org/10.33263/BRIAC101.706713.
36. Tanhaei, B.; Ayati, A.; Iakovleva, E.; Sillanpää, M. Efficient carbon interlayed magnetic chitosan adsorbent for anionic dye removal: Synthesis, characterization and adsorption study. *Int. J. Biol. Macromol.* **2020**, *164*, 3621-3631, https://doi.org/10.1016/j.ijbiomac.2020.08.207.
37. Al Bsoul, A. Efficient removal of phenol compounds from water environment using Ziziphus leaves adsorbent. *Sci. Total Environ*. **2021**, *761*, 143229, https://doi.org/10.1016/j.scitotenv.2020.143229.
38. Kyzas, G.Z.; McKay, G.; Al-Musawi, T.J.; Salehi, S.; Balarak, D. Removal of Benzene and Toluene from Synthetic Wastewater by Adsorption onto Magnetic Zeolitic Imidazole Framework Nanocomposites. *Nanomaterials* **2022**, *12*, 3049, https://www.mdpi.com/2079-4991/12/17/3049.
39. Naguib, D. M.; & Badawy, N. M. Phenol removal from wastewater using waste products. *J. Environ. Chem. Eng*. **2020**, *8*, 103592, https://doi.org/10.1016/j.jece.2019.103592.
40. Supong, A. Experimental and theoretical insight into the adsorption of phenol and 2,4-dinitrophenol onto Tithonia diversifolia activated carbon. *Appl. Surf. Sci.* **2020**, *529*, 147046, https://doi.org/10.1016/j.apsusc.2020.147046.
41. Mohammadi, L.; Baniasadi, M.; Rahdar, A.; Kyzas, G.Z. Removal of Acid Dye from Aqueous Solutions with Adsorption onto Modified Wheat Bran –Modeling with Artificial Neural Networks. *Biointerface Res. Appl. Chem*. **2021**, *11*, 14044-14056, https://biointerfaceresearch.com/wp-content/uploads/2021/03/20695837116.1404414056.pdf.
42. Egbosiuba, T. C. Ultrasonic enhanced adsorption of methylene blue onto the optimized surface area of activated carbon: Adsorption isotherm, kinetics and thermodynamics. *Chem. Eng. Res. Des.* **2020**, *153*, 315–336, https://doi.org/10.1016/j.cherd.2019.10.016.
43. Anuar, F.I.; Hadibarata, T.; Syafrudin, M.; Fona, Z. Removal of Procion Red MX- 5B from aqueous solution by adsorption on Parkia speciosa (stink bean) peel powder. *Biointerface Res. Appl. Chem*. **2020**, *10*, 4774–4779, https://doi.org/10.33263/BRIAC101.774779.
44. Khalil, K.M.S.; Khairy, M.; Allam, O.A.S. Formation of improved activated carbons from sugarcane bagasse as environmental materials for adsorption of phenolic pollutants. *Int. J. Environ. Sci. Technol*. **2022**, *19*, 3103–3116, https://doi.org/10.1007/s13762-021-03382-3.
45. Altowayti, W.A.H.; Haris, S.A.; Almoalemi, H.; Shahir, S.; Zakaria, Z.; Ibrahim, S. The removal of arsenic species from aqueous solution by indigenous microbes: Batch bioadsorption and artificial neural network model. *Environ. Technol. Innovation.* **2020**, *19*, https://doi.org/10.1016/j.eti.2020.100830.

46. Alalwan, H.A.; Kadhom, M.A.; Alminshid, A.H. Removal of heavy metals from wastewater using agricultural byproducts. *J. Water. Supply: Res. Technol. Aqua* **2020**, *69*, 99-112, https://doi.org/10.2166/aqua.2020.133.
47. Lindner, A.V.; Pleissner, D. Removal of Phenolic Compounds from Olive Mill Wastewater by Microalgae Grown Under Dark and Light Conditions. *Waste Biomass Valor.* **2022**, *13*, 525–534, https://doi.org/10.1007/s12649-021-01536-5.
48. Rout, D.R., Jena, H.M. Removal of phenol from aqueous solution using reduced graphene oxide as adsorbent: isotherm, kinetic, and thermodynamic studies. *Environ Sci Pollut Res*. **2022**, *29*, 32105–32119, https://doi.org/10.1007/s11356-021-17944-y.
49. Ahmadi, S.; Mohammadi, L.; Rahdar, A.; Rahdar, S.; Dehghani, R.; Adaobi Igwegbe, C.; Kyzas, G.Z. Acid Dye Removal from Aqueous Solution by Using Neodymium(III) Oxide Nanoadsorbents. *Nanomaterials* **2020**, *10*, https://doi.org/10.3390/nano10030556.
50. Eryılmaz, C.; Genç, A. Review of Treatment Technologies for the Removal of Phenol from Wastewaters. *J. Water Chem. Technol*. **2021**; *43*, 145–154, https://doi.org/10.3103/S1063455X21020065.
51. Dargahi, A.; Samarghandi, M.R.; Shabanloo, A. Statistical modeling of phenolic compounds adsorption onto low-cost adsorbent prepared from aloe vera leaves wastes using CCD-RSM optimization: effect of parameters, isotherm, and kinetic studies. *Biomass Conv. Bioref.* **2021**. *11*, 1-11, https://doi.org/10.1007/s13399-021-01601-y
52. Othmani, A.; Kesraoui, A.; Seffen, M. Removal of phenol from aqueous solution by coupling alternating current with biosorption. *Environ Sci Pollut Res*. **2021**, *28*, 46488–46503, https://doi.org/10.1007/s11356-020-09976-7.
53. Kittappa, S.; Jais, F.M.; Ramalingam, M.; Mohd, N.S.; Ibrahim, S. Functionalized magnetic mesoporous palm shell activated carbon for enhanced removal of azo dyes. *J. Environ. Chem. Eng*. **2020**, *8*, https://doi.org/10.1016/j.jece.2020.104081.
54. De Benedetto, C.; Macario, A.; Siciliano, C.; B. Nagy, J.; De Luca, P. Adsorption of Reactive Blue 116 Dye and Reactive Yellow 81 Dye from Aqueous Solutions by Multi-Walled Carbon Nanotubes. *Materials* **2020**, *13*, https://doi.org/10.3390/ma13122757.
55. Kuang, Y.; Zhang, X.; Zhou, S. Adsorption of methylene blue in water onto activated carbon by surfactant modification. *Water* **2020**, *12*, 87-93, https://doi.org/10.3390/w12020587.
56. Ambaye, T.G.; Vaccari, M.; Hullebusch, E. D. Mechanisms and adsorption capacities of biochar for the removal of organic and inorganic pollutants from industrial wastewater. *Int. J. Environ. Sci. Technol.* **2021**, *18*, 3273–3294, https://doi.org/10.1007/s13762-020-03060-w. .